

# Revisiting the A-type antiferromagnet $\text{NaNiO}_2$ with muon spin rotation measurements and density functional theory calculations

Ola Kenji Forslund <sup>1,\*</sup>, Hiroto Ohta <sup>2,3</sup>, Kazuya Kamazawa,<sup>4</sup> Scott L. Stubbs,<sup>5</sup> Oren Ofer,<sup>6</sup> Martin Månsson <sup>1</sup>, Chishiro Michioka,<sup>3</sup> Kazuyoshi Yoshimura,<sup>3</sup> Bassam Hitti,<sup>6</sup> Donald Arseneau <sup>6</sup>, Gerald D. Morris,<sup>6</sup> Eduardo J. Ansaldo,<sup>7</sup> Jess H. Brewer <sup>5,6</sup> and Jun Sugiyama <sup>4,8,9,†</sup>

<sup>1</sup>Department of Applied Physics, KTH Royal Institute of Technology, SE-10691 Stockholm, Sweden

<sup>2</sup>Engineering Education Research Center, Graduate School of Engineering, Kyoto University, Kyoto 615-8530, Japan

<sup>3</sup>Department of Chemistry, Graduate School of Science, Kyoto University, Kyoto 606-8502, Japan

<sup>4</sup>CROSS Neutron Science and Technology Center, Tokai, Ibaraki 319-1106, Japan

<sup>5</sup>Department of Physics & Astronomy, University of British Columbia, Vancouver, British Columbia, Canada V6T 1Z1

<sup>6</sup>TRIUMF, 4004 Wesbrook Mall, Vancouver, British Columbia, Canada V6T 2A3

<sup>7</sup>Department of Physics & Engineering Physics, University of Saskatchewan, Saskatoon, Saskatchewan, Canada S7N 5E2

<sup>8</sup>Advanced Science Research Center, Japan Atomic Energy Agency, Tokai, Ibaraki 319-1195, Japan

<sup>9</sup>High Energy Accelerator Research Organization (KEK), Tokai, Ibaraki 319-1106, Japan

 (Received 15 June 2020; revised 8 October 2020; accepted 26 October 2020; published 11 November 2020)

An A-type antiferromagnet,  $\text{NaNiO}_2$ , was examined by means of positive muon spin rotation and relaxation ( $\mu^+$ SR) measurements and first-principles calculations based on a density functional theory (DFT). Below  $T_N = 20$  K, a clear muon spin precession signal was observed in the  $\mu^+$ SR time spectrum recorded under zero field, due to the formation of a static internal magnetic field. The microscopic origin of such an internal field was computed as a sum of dipolar and hyperfine contact fields at the site (0.624, 0, 0.854), where both the muon site and the local spin density at such a site were predicted with DFT calculations. While the computed values were consistent with experimentally obtained ones, in both the antiferromagnetic and the paramagnetic states, the contribution of the hyperfine contact field was shown to be insignificant even below  $T_N$ . Finally, measurements at higher temperatures signified thermally activated Na-ion diffusion with  $E_a = 50(20)$  meV and  $D_{\text{Na}}(300\text{ K}) = 8.8 \times 10^{-11}$  cm<sup>2</sup>/s, commonly observed in layered-type compounds.

DOI: [10.1103/PhysRevB.102.184412](https://doi.org/10.1103/PhysRevB.102.184412)

## I. INTRODUCTION

The positive muon spin rotation and relaxation ( $\mu^+$ SR) technique is widely used for studying the local magnetic environments in various magnetic compounds [1–3]. The implanted spin-polarized  $\mu^+$  sits at an interstitial site where the electrostatic potential is minimal, which is usually close to an anion at a distance of around 1 Å [4]. The muon possesses a gyromagnetic ratio ( $\gamma_\mu$ ), which in the presence of a magnetic field results in spin precession according to the local magnetic field at the muon site ( $\mathbf{B}_{\text{loc}}$ ). For nonmagnetic, paramagnetic (PM), and the majority of antiferromagnetic (AF) materials,  $\mathbf{B}_{\text{loc}}$  is mainly formed by dipolar fields ( $\mathbf{B}_{\text{dip}}$ ) caused by nuclear and electron magnetic moments. For these materials, the information obtained by  $\mu^+$ SR is well explained as a source of

$\mathbf{B}_{\text{dip}}$ , which is defined by the magnitude of magnetic moments, the distribution of magnetic moments, and the magnetic structure.

For ferromagnetic (FM) and ferrimagnetic materials in the zero applied field, there are two additional contributions to  $\mathbf{B}_{\text{loc}}$ :

$$\mathbf{B}_{\text{loc}} = \mathbf{B}_{\text{dip}} + \mathbf{B}_L + \mathbf{B}_{\text{hf}}. \quad (1)$$

One is the Lorentz field ( $\mathbf{B}_L$ ), which comes from the magnetic field caused by the dipoles beyond the consideration range for  $\mathbf{B}_{\text{dip}}$  [5].  $\mathbf{B}_{\text{dip}}$  has a simple analytical form and  $\mathbf{B}_L$  is proportional to the macroscopic magnetization and is easily obtained in magnetization measurements. The other is the hyperfine contact field ( $\mathbf{B}_{\text{hf}}$ ), which arises due to short-range interaction between the  $\mu^+$  spin and the local spin at the muon site, because the local spin density in magnetically ordered materials is usually nonzero, especially for ferro- and ferrimagnets. While  $\mathbf{B}_{\text{hf}}$  is typically significant in conducting materials, due to the coupling between polarized conduction electrons and the muon, local polarized electrons will contribute to  $\mathbf{B}_{\text{hf}}$  as well, like in the ferromagnetic semiconductor  $\text{EuO}$  [6] or the insulator  $\text{K}_2\text{Cr}_8\text{O}_{16}$  [7]. By similar arguments, the local field of A-type antiferromagnets is described by the terms  $\mathbf{B}_{\text{dip}}$ ,  $\mathbf{B}_L = 0$ , and possibly with a nonzero  $\mathbf{B}_{\text{hf}}$ , depending on the muon site, given that the magnetic moments align

\*okfo@kth.se

†juns@triumf.ca

Published by the American Physical Society under the terms of the [Creative Commons Attribution 4.0 International](https://creativecommons.org/licenses/by/4.0/) license. Further distribution of this work must maintain attribution to the author(s) and the published article's title, journal citation, and DOI. Funded by *Bibsam*.

ferromagnetically in the plane but antiferromagnetically between the adjacent planes. Therefore, the muon site and the local spin density need to be considered in  $\mu^+$ SR measurements for the three magnetic materials mentioned. Given that  $\mathbf{B}_{\text{hf}}$  is usually considered small and requires density functional theory (DFT) computation, it is a common practice to omit this contribution when evaluating the internal field in AF material. However, since a ferromagnetic coupling exists within the crystallographic plane, this begs the question of whether such an approximation is valid even for A-type antiferromagnetic compounds, where one could perhaps expect significant local spin density at the local muon site.

Recent progress in DFT calculations has enabled the prediction of not only the muon sites but also the local spin density at such sites. A first attempt to analyze  $\mu^+$ SR data of a ferromagnet with the help of such DFT calculations has been carried out for a well-known permanent magnet,  $\text{Nd}_2\text{Fe}_{14}\text{B}$ , and has clarified the magnitude of the ordered Nd moment [8]. As a second attempt, we here report the  $\mu^+$ SR result on the A-type antiferromagnet,  $\text{NaNiO}_2$ . It is noted that  $\mu^+$ SR results of  $\text{NaNiO}_2$  have already been reported [9] but without the abovementioned detailed analysis.

Figure 1 shows the crystal structure of  $\text{NaNiO}_2$ , which consists of alternating Na layers and single  $\text{CdI}_2$ -type  $\text{NiO}_2$  layers, stacked along the  $c$  axis. In the  $\text{NiO}_2$  plane, a two-dimensional triangular lattice of  $\text{Ni}^{3+}$  ions is formed by a network of edge-sharing  $\text{NiO}_6$  octahedra [11]. The electron configuration of the  $\text{Ni}^{3+}$  ion is in a low-spin state with  $t_{2g}^6 e_g^1$  ( $S = 1/2$ ) in the crystalline field of the  $\text{NiO}_6$  octahedron [12]. This naturally leads to an interest in the magnetic ground state of  $\text{NaNiO}_2$  from the viewpoint of geometrical frustration.  $\text{NaNiO}_2$  exhibits two transitions at  $T_{\text{JT}} = 480$  K and  $T_{\text{N}} = 20$  K [13,14]. The former is a cooperative Jahn-Teller (JT) transition from a high-temperature rhombohedral phase with space group  $R\bar{3}m$  to a low-temperature monoclinic phase with space group  $C2/m$ , while the latter is a transition into an A-type AF phase, i.e., an FM order in the  $\text{NiO}_2$  plane but AF between the two adjacent  $\text{NiO}_2$  planes. Such a spin structure was first suggested by a high magnetic field experiment [13] but then later confirmed in a neutron diffraction experiment [14]. Additionally, the detailed study showed that the moments were aligned in the  $ac$  plane, with an angle of  $100^\circ$  with respect to the  $a$  axis. Such an A-type AF order is associated with the JT induced trigonal distortion which stabilizes a half-occupied  $d_{z^2}$  orbital [15].

Besides the interests in the abovementioned magnetic nature,  $\text{NaNiO}_2$  has been investigated as a cathode material for a Na-ion battery [16–20]. Recently, it was proposed that the Jahn-Teller distortion enhances Na diffusion in the  $\text{NaNiO}_2$  lattice [21], based on first-principles calculations [22]. However, the presence of paramagnetic Ni ions in the lattice makes it difficult to measure Na diffusion with Na NMR [23,24]. Therefore, we have also measured the  $\mu^+$ SR spectra up to 250 K in order to study the dynamics of the nuclear magnetic field [25] mainly formed by  $^{23}\text{Na}$ .

## II. EXPERIMENTAL METHODS

A polycrystalline sample of  $\text{NaNiO}_2$  was synthesized by a solid-state reaction technique. Powders of  $\text{Na}_2\text{O}_2$  and  $\text{NiO}$

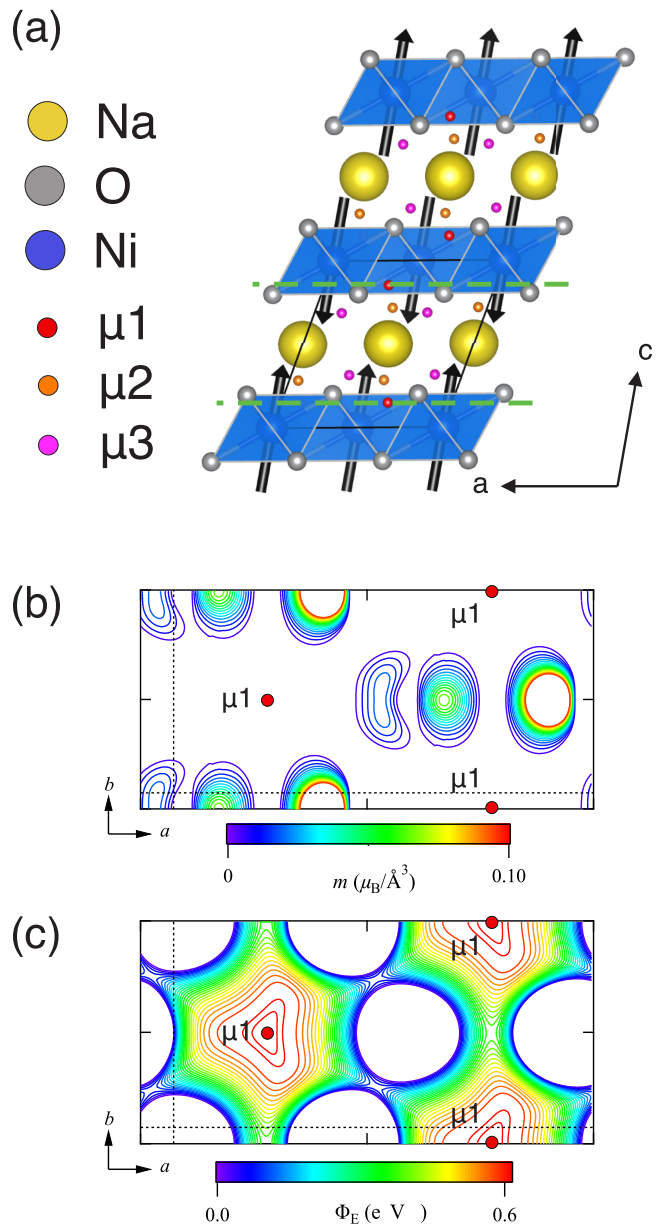


FIG. 1. (a) Magnetic structure of  $\text{NaNiO}_2$  drawn by VESTA [10]. The predicted muon sites by DFT calculations are indicated as spheres: red  $\mu 1$  at  $(0.624, 0, 0.854)$ , orange  $\mu 2$  at  $(0.9467, 0, 0.28)$ , and magenta  $\mu 3$  at  $(0.84, 0.225, 0.69)$ . The coordinates are specified for the crystal space group  $C2/m$  with setting  $C2/m$  (unique  $b$  axis):  $a = 5.30811$ ,  $b = 2.84193$ ,  $c = 5.56671$  \AA, and  $\beta = 110.4503^\circ$ . The magnetic moments are indicated as black arrows. Contour maps of spin density (b) and Coulomb potential (c) for  $U = 3.6$  eV are shown for a plane cut at  $z = 0.854$ , i.e., through the  $\mu 1$  site. Such a plane cut is shown as a dashed green line in panel (a). The horizontal and vertical dotted black lines indicate the unit cell boundaries.

were mixed in the ratio of 1.1:2 and pelletized in an Ar atmosphere. The pelletized disk was heated at  $700^\circ\text{C}$  in an  $\text{O}_2$  gas flow for 27 h. This heating process was repeated after an intermediate grinding. The obtained sample was confirmed as a single phase of  $\text{NaNiO}_2$  by powder x-ray diffraction measurements.

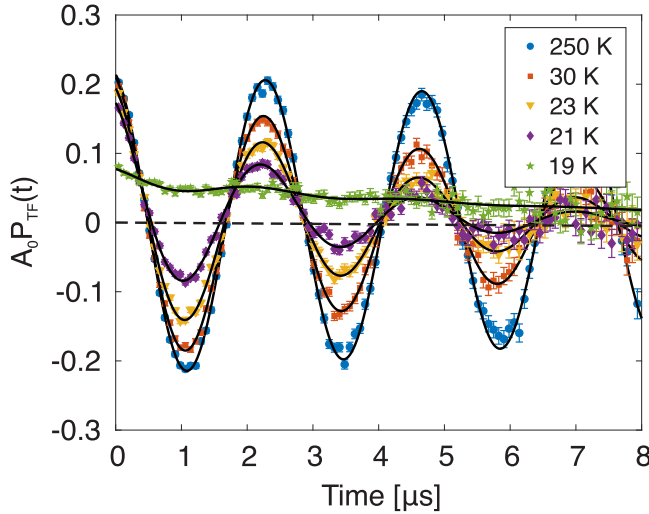


FIG. 2. Transverse field (TF) time spectra recorded at  $T = 19, 21, 23, 30,$  and  $250$  K. The solid lines represent fits using Eq. (2).

The  $\mu^+$ SR measurements were performed on the M20 surface muon beam line using the LAMPF spectrometer of the CMMS facility at TRIUMF in Canada. A sample disk 15 mm in diameter and 3 mm in thickness was mounted on a Cu fork sample holder with Mylar tape. A standard  $^4\text{He}$  flow cryostat was used to reach the lowest temperature  $T_{\text{base}} = 2$  K. The software MUSRFIT [26] was used in order to analyze the  $\mu^+$ SR data.

In order to estimate muon sites and spin densities at the muon sites, first-principles DFT calculations were performed using the full-potential linearized augmented plane wave method within the local spin-density approximation +  $U$  method as implemented in the WIEN2K program package [27]. In the calculations, the lattice parameters and atomic positions of  $\text{NaNiO}_2$  were taken from Ref. [14], and  $U$  for Ni was taken from Ref. [28] to be 3.6 eV. The muffin tin potential radii for Na, Ni, and O were taken to be 2.18, 1.93, and 1.66 Å, respectively. Since this is the first attempt to study the effect of local spin density on  $\mathbf{B}_{\text{loc}}$  at the muon sites, we use a conservative approach for the DFT calculations. That is, although the implanted  $\mu^+$  is known to distort the local structural environments [29], such distortion is ignored. This is because it is difficult to predict the local spin density under such distorted conditions.

### III. RESULTS

The  $\mu^+$ SR measurements were performed under three different field configurations: zero field (ZF), longitudinal field (LF), and transverse field (TF). LF and TF refer to the applied field directions, namely, parallel and perpendicular with respect to the initial muon spin polarization.

#### A. Transverse field

Transverse field (TF = 30 G) time spectra at selected temperatures are displayed in Fig. 2. A clear precession of about 0.4 MHz, which corresponds to 30 G, and a slowly relaxing offset signal are seen. Therefore, the TF time spectra were

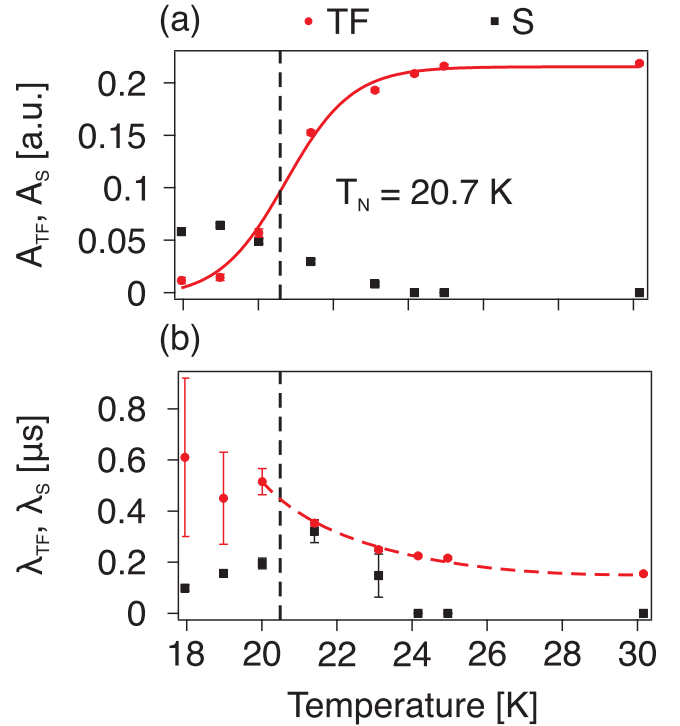


FIG. 3. Temperature dependence of fit parameters obtained using Eq. (2): (a) asymmetries ( $A_{\text{TF}}$  and  $A_S$ ) and (b) relaxation rates ( $\lambda_{\text{TF}}$  and  $\lambda_S$ ). The solid line corresponds to a fit with a sigmoidal function, whereas the dotted line is a guide to the eye. The dotted vertical lines across the figures indicate the transition temperature  $T_N^{\text{TF}} = 20.73(6)$  K.

fitting by a combination of an exponentially relaxing oscillatory component and an exponentially relaxing nonoscillatory component:

$$A_0 P_{\text{TF}}(t) = A_{\text{TF}} \cos(f_{\text{TF}} 2\pi t + \phi_{\text{TF}}) \exp(-\lambda_{\text{TF}} t) + A_S \exp(-\lambda_S t), \quad (2)$$

where  $A_0$  is the initial total asymmetry and  $P_{\text{TF}}$  is the muon spin polarization function under TF.  $A_{\text{TF}}$ ,  $f_{\text{TF}}$ ,  $\phi_{\text{TF}}$ , and  $\lambda_{\text{TF}}$  are the asymmetry, frequency, initial phase, and relaxation rate resulting from the applied TF, respectively.  $A_S/A_0$  represents the fraction of muon polarization initially parallel to the local magnetic field, and  $\lambda_S$  is proportional to the fluctuation rate of the paramagnetic moments, causing the local field to change direction.

Some of the obtained fit parameters are displayed in Fig. 3. Each asymmetry exhibits a temperature dependence expected for a magnetically ordered sample. At higher temperatures,  $A_{\text{TF}}$  is close to full asymmetry, meaning that the sample is entirely paramagnetic. At lower temperature on the other hand,  $A_{\text{TF}}$  is close to 0, indicating that the applied TF is much weaker than the internal field. Since  $A_{\text{TF}}/A_0$  roughly corresponds to the paramagnetic volume fraction of the sample, the decrease in  $A_{\text{TF}}/A_0$  evidences the transition from a paramagnetic state to a magnetically ordered state. A sigmoidal fit of the  $A_{\text{TF}}(T)$  curve yields a transition temperature of  $T_N^{\text{TF}} = 20.73(6)$  K. As  $A_{\text{TF}}$  decreases with decreasing temperature from 30 K,  $A_S$  increases instead and levels off to about 1/3 of

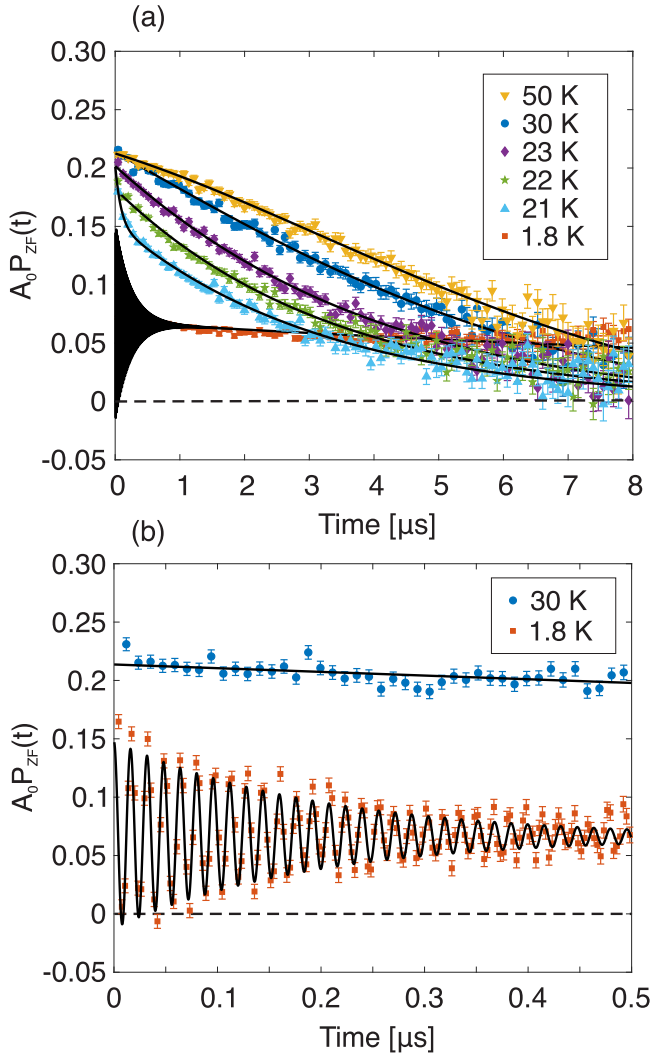


FIG. 4. Zero field (ZF) time spectra recorded at  $T = 2\text{--}50$  K, showing the long time domain up to (a)  $8\ \mu\text{s}$  and (b)  $0.5\ \mu\text{s}$  (b). The solid lines are fits obtained using Eq. (3).

$A_0$  at temperatures below  $T_N$ , because  $A_S$  corresponds roughly to the  $1/3$  tail signal, as described later.

The two relaxation rates exhibit small anomalies around  $T_N^{\text{TF}}$ . As temperature decreases from 30 K,  $\lambda_{\text{TF}}$  steadily increases and shows a maximum at  $T_N^{\text{TF}}$ . The values below  $T_N^{\text{TF}}$  are inaccurate given the small asymmetry available. On the other hand,  $\lambda_S$  shows a temperature dependence roughly similar to that of  $\lambda_{\text{TF}}$ , but clearly decreases with further decreasing temperature below  $T_N^{\text{TF}}$ . These behaviors reflect broadening of the internal field distribution seen in magnetic transitions. A more accurate trend of the dynamics around  $T_N^{\text{TF}}$  is obtained in ZF measurements, as described in Sec. III B.

### B. Zero field

Figure 4 shows the  $\mu^+$ SR time spectrum for  $\text{NaNiO}_2$  recorded under zero field (ZF) at selected temperatures. A clear oscillation is observed below  $T_N^{\text{TF}}$  while an exponential-like relaxation without an oscillation is instead seen at higher temperatures, which develops into a more Gaussian-like re-

laxation at temperatures  $>50$  K. More precisely, the  $\mu^+$ SR spectrum in the paramagnetic state is modeled with a product of an exponential relaxation and a dynamic Gaussian Kubo-Toyabe (DGKT) [30]. The response of a muon ensemble originating from two independent sources of magnetic field distributions is given by the Fourier transform of their convolution. Thus, the response can be modeled as a product of an exponential relaxation, originating from a fluctuating Ni  $3d$  moment, and a DGKT, originating from a fluctuating nuclear magnetic field. In DGKT,  $\Delta$  is the internal field distribution width and  $\nu$  is the field fluctuation rate caused by nuclear magnetic moments, mainly from  $I_{\text{Na}} = 3/2$ . As the temperature is lowered, however, the nuclear contribution to the time spectrum becomes insignificant compared to the fluctuating paramagnetic moments and the response of the muon ensemble becomes more exponential like. Therefore, the ZF time spectrum, from low to high temperature, was fitted by a combination of an exponentially relaxing cosine component, an exponentially relaxing nonoscillatory component, and an exponentially relaxing DGKT component:

$$A_0 P_{\text{ZF}}(t) = A_{\text{AF}} \cos(f_{\text{AF}} 2\pi t + \phi) \exp(-\lambda_{\text{AF}} t) + A_{\text{tail}} \exp(-\lambda_{\text{tail}} t) + A_{\text{KT}} G^{\text{DGKT}}(H_{\text{LF}}, \Delta, \nu, t) \exp(-\lambda_{\text{KT}} t), \quad (3)$$

where  $A_0$  is the initial asymmetry and  $P_{\text{ZF}}$  is the muon spin polarization function under ZF, i.e.,  $H_{\text{LF}} = 0$ .  $A_{\text{AF}}$ ,  $f_{\text{AF}}$ ,  $\phi$ , and  $\lambda_{\text{AF}}$  are the asymmetry, frequency, initial phase, and relaxation rate, respectively, arising from internal field components that are perpendicular to the initial muon spin polarization.  $A_{\text{tail}}$  and  $\lambda_{\text{tail}}$  are the asymmetry and the relaxation rate of the so-called ‘‘tail component,’’ arising from the internal field contributions that are parallel to the initial muon spin polarization. In a random powder antiferromagnet,  $1/3$  of the magnetic contribution results in a tail while the rest,  $2/3$ , yields oscillation. Since  $A_0 \simeq 0.21$ , the value of  $A_{\text{tail}}(2\text{ K}) = 0.068$  is reasonable for the tail component. However, the total asymmetry ( $A_{\text{tail}} + A_{\text{AF}}$ ) at 2 K is about 0.15, and thus, there is a missing asymmetry of about  $A_{\text{missing}} = 0.06$  (see the Appendix).

Such missing asymmetry is likely to be seen in the past  $\mu^+$ SR work on  $\text{NaNiO}_2$  obtained in Paul Scherrer Institute (PSI) [9], judging from the reported ZF  $\mu^+$ SR spectrum. Therefore, the missing asymmetry is not sample and/or facility dependent but rather is an intrinsic feature of  $\text{NaNiO}_2$ . A missing asymmetry is usually caused by either a muonium ( $\mu^+e^-$ ) formation [31–34] or the presence of quasistatic wide field distributions, i.e., fields and frequencies too high to be resolved by  $\mu^+$ SR. Muonium formation is commonly observed in insulating and/or semiconducting compounds. While  $\text{NaNiO}_2$  exhibits a semiconducting behavior above room temperature [35], resistivity measurements at lower temperatures are unavailable. That being said, since full asymmetry is observed above  $T_N$ , or more correctly at 25 K, a muonium scenario is highly unlikely in  $\text{NaNiO}_2$ . Instead, this missing asymmetry originates from muons sensing high fields and wide field distributions, such that it cannot be resolved by the  $\mu^+$ SR technique. Of course, such a scenario implies that about 20% of the implanted  $\mu^+$ s are located at a site more proximate to Ni than the predicted

TABLE I. The predicted muon sites and their respective local spin density  $\rho(r_\mu)$ . The calculated values of  $f_{\text{dip}'}$  and  $f_{\text{loc}}$  using Eqs. (5)–(7), the experimentally obtained  $f_{\text{AF}}(0)$ , and their corresponding magnetic fields are tabulated. Here,  $f_{\text{dip}'}$  =  $(\gamma_\mu/2\pi)|\mathbf{B}_{\text{dip}'}|$  and  $f_{\text{loc}}$  =  $(\gamma_\mu/2\pi)|\mathbf{B}_{\text{dip}' + \mathbf{B}_{\text{hf}}}|$ , where  $\mathbf{B}_{\text{hf}} = \frac{2\mu_0}{3} \frac{\rho(r_\mu)}{|m_e|} \mathbf{m}_e$  and  $\mu_0 = 4\pi \times 10^{-7}$  H/m.  $\Delta_{\text{NaNiO}_2}^{\text{calc}}$  for each site is also included.

| Muon site                   | $\rho(r_\mu)$ ( $\mu_B \text{\AA}^{-3}$ ) | $\mathbf{B}_{\text{dip}'}$ (G) | $\mathbf{B}_{\text{hf}}$ (G) | $f_{\text{dip}'}$ (MHz) | $f_{\text{loc}}$ (MHz) | $f_{\text{AF}}(0)$ (MHz) | $\Delta_{\text{NaNiO}_2}^{\text{calc}}$ ( $\mu\text{s}^{-1}$ ) |
|-----------------------------|---|--------------------------------|------------------------------|-------------------------|------------------------|--------------------------|--|
| $\mu 1$ (0.624, 0, 0.854)   | $8.122 \times 10^{-5}$                    | [−597, 0, −4380]               | [−1, 0, 6]                   | 59.91<br>(4420 G)       | 59.83<br>(4414 G)      | 65.1(6)<br>[4802(44) G]  | 0.177<br>(2.076 G)   |
| $\mu 2$ (0.9467, 0, 0.28)   | −0.003127                                 | [−1863, 0, 712]                | [44, 0, −239]                | 27.04<br>(1995 G)       | 25.48<br>(1880 G)      | 65.1(6)<br>[4802(44) G]  | 0.244<br>(2.868 G)   |
| $\mu 3$ (0.84, 0.225, 0.69) | 0.003471                                  | [611, −1107, 675]              | [−49, 0, 265]                | 19.43<br>(1434 G)       | 21.11<br>(1557 G)      | 65.1(6)<br>[4802(44) G]  | 0.259<br>(3.042 G)   |

sites (see Fig. 1 and Table I). Here, the  $\mu 1$  site is located in the  $\text{NiO}_2$  plane but outside the  $\text{NiO}_6$  octahedron. This suggests that the more proximate site should be located inside the  $\text{NiO}_6$  octahedron. Such a site would result in higher fields and wider field distributions, resulting in a relaxation not resolvable with  $\mu^+$ SR.

The temperature dependencies of the fit parameters obtained using Eq. (3) are displayed in Fig. 5. A small shift of  $\phi \simeq 30^\circ$  was observed at the base temperature. However,  $\phi = 0$  was set as the sample and is known to have a commensurate AF order and phase shifts are instead commonly observed in incommensurate orders (IC), meaning small values of  $\phi \simeq 0^\circ$  are expected for the title compound. As the temperature increases, the AF field distribution in the sample usually becomes wider. Such wide distribution is sometimes not appropriate for being fitted with an exponentially relaxing cosine function with  $\phi = 0$  and nonzero values are obtained at the vicinity of  $T_N$  [Fig. 5(d)]. The obtained nonzero  $\phi$  in such a situation is, however, not an intrinsic feature of the AF phase.

A transition from a low-temperature AF state to a high-temperature PM state is clearly observed. Most prominently, the temperature dependence of  $f_{\text{AF}}(T)$  exhibits an order parameterlike behavior, as seen in Fig. 5(c). The phenomenological expression  $f_{\text{AF}}(T) = f_{\text{AF}}(0)(1 - T/T_N^{\text{ZF}})^\beta$  is nicely fitted to the  $f_{\text{AF}}(T)$  curve. Such a fit yields  $f_{\text{AF}}(0) = 65.1(6)$  MHz,  $\beta = 0.279(7)$ , and  $T_N^{\text{ZF}} = 20.09(1)$  K. The value of  $T_N^{\text{ZF}}$  is consistent with the value of  $T_N^{\text{TF}}$ .

The asymmetry components in Fig. 5(a) show a temperature-independent behavior at low temperatures. Closer to  $T_N^{\text{ZF}}$ , a small increase in  $A_{\text{AF}}$  is seen, which could perhaps be explained by part of  $A_{\text{Missing}}$  entering the time window of  $\mu^+$ SR. Above the transition,  $A_{\text{AF}}$  goes to the zero and the signal is taken over by  $A_{\text{KT}}$ , which reaches a value close to  $A_0$ . The increase of  $\lambda_{\text{AF}}$  around  $T_N^{\text{ZF}}$  is also consistent with an increase of internal field distribution, as commonly seen in magnetic transitions.

As the temperature increases from 2 K,  $\lambda_{\text{tail}}$  increases linearly up to  $T_N^{\text{ZF}}$ . Since  $\lambda_{\text{tail}}$  corresponds to the spin-lattice relaxation rate, the increase is understood from the increase in the dynamics of the internal fields. Given that  $\lambda_{\text{tail}}(2 \text{ K}) \simeq 0.05 \mu\text{s}^{-1}$ , a small dynamic contribution is expected even at low temperature. Above  $T_N^{\text{ZF}}$ ,  $\lambda_{\text{KT}}$  exhibits a maximum and reflects the critical slowdown of Ni moments, as the temperature is lowered. The temperature dependence of  $\lambda_{\text{KT}}$  at higher temperatures is explained in Sec. III C. The ZF  $\mu^+$ SR results presented in Sec. III B are in good agreement with those of a

previous publication [9], apart from the discussion regarding the missing fraction (see the Appendix).

### C. Longitudinal field

The  $\mu^+$ SR spectrum was also recorded under longitudinal fields (LF) of  $H_{\text{LF}} = 5, 10, 20,$  and  $40$  G above  $T = 30$  K. ZF and LF  $\mu^+$ SR time spectra collected at 50 and 150 K are shown in Fig. 6. A clear reduction in the relaxation rate is seen at higher temperature, suggesting an increase in internal magnetic field dynamics. Since the sample is PM above  $T_N^{\text{ZF}}$ , the time spectra are nicely fitted using Eq. (3) with  $A_{\text{AF}} = A_{\text{tail}} = 0$ . The ZF and LF  $\mu^+$ SR spectra were fitted using a common  $A_{\text{KT}}$  in the whole temperature range measured and a common  $\lambda_{\text{KT}}, \Delta,$  and  $\nu$  at each temperature. Here, we assume that the spin-spin correlations are not affected for  $H_{\text{LF}}$  up to  $\sim 40$  G. The temperature dependencies of the fit parameters are shown in Fig. 7. At temperatures above  $T = 30$  K,  $\lambda_{\text{KT}}$  decreases with temperature like the temperature dependence of magnetic susceptibility in a Curie-Weiss paramagnet. This suggests that the paramagnetic fluctuation of the Ni moments increases with the temperature, which eventually become motionally narrowed, limited by the  $\mu^+$ SR time window.

As the temperature increases from 30 K,  $\Delta$  is almost temperature independent up to about 150 K, because the fluctuations of nuclear moments are static within the muon lifetime, i.e., quasistatic. Indeed, using the Van Vleck formalism, calculation of the internal field distribution stemming from nuclear moments at site  $\mu 1$  at (0.624, 0, 0.854) yields  $\Delta_{\text{NaNiO}_2}^{\text{calc}} = 2.076$  G, which corresponds to  $0.177 \mu\text{s}^{-1}$ . While a small difference compared to the experimental value is seen, the calculated value is consistent with the observed  $\Delta$  below 150 K. The small difference stems most likely from local lattice distortions the implanted muon induces, which effectively change the distances between the muon and the surrounding atoms and such distortions were not considered in the calculation. Around 150 K on the other hand,  $\Delta$  exhibits an abrupt decrease together with an increase in  $\nu$ . Such behavior is most likely caused by Na diffusion, which should occur in  $\text{NaNiO}_2$  based on electrochemical properties. In fact, similar layered compounds, such as  $\text{Na}_x\text{CoO}_2$  [36],  $\text{Li}_x\text{CoO}_2$  [25], and  $\text{LiNiO}_2$  [37,38] also show a thermally activated ion diffusion at similar or higher temperatures, resulting in a decrease of  $\Delta$  as the  $\nu$  increases. For  $\text{Na}_x\text{CoO}_2$ , furthermore, such a diffusive behavior detected with  $\mu^+$ SR is consistent with the results obtained by Na NMR [39] and neutron diffraction [40] measurements and electron diffraction observations [41].

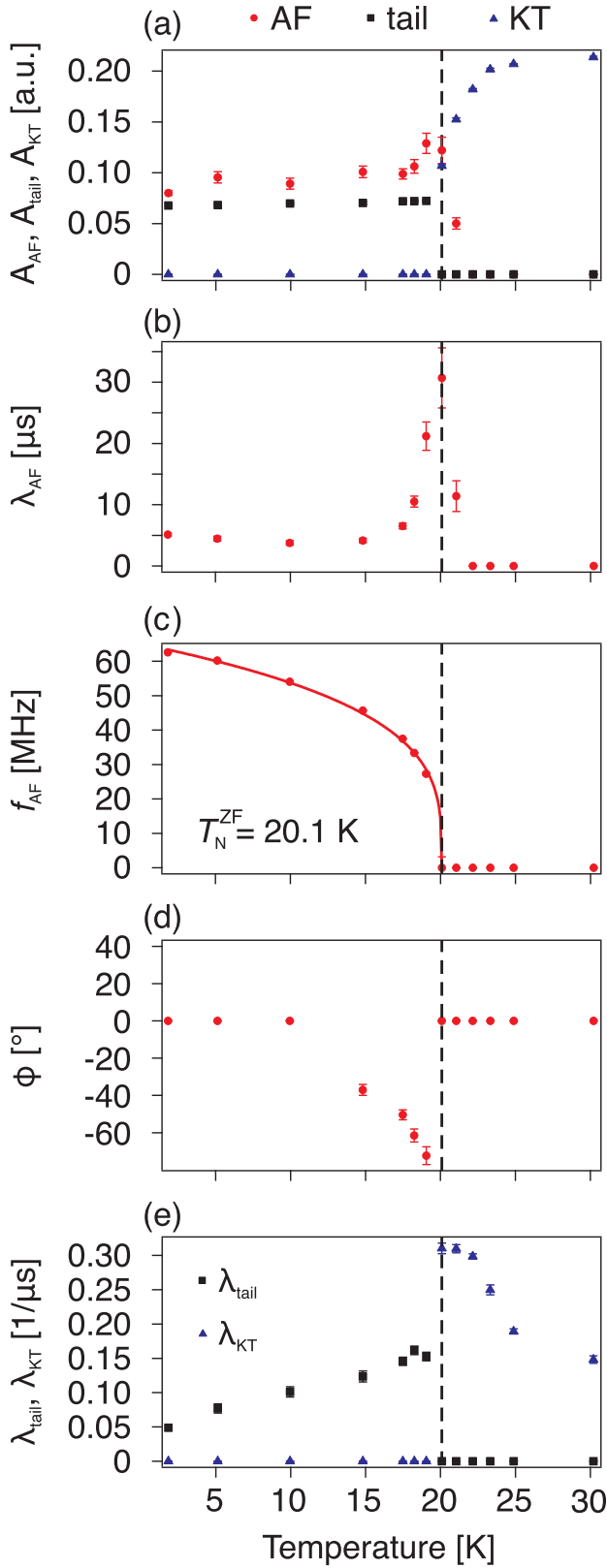


FIG. 5. Temperature dependencies of the fit parameters obtained with Eq. (3): (a) asymmetries ( $A_{AF}$ ,  $A_{tail}$ , and  $A_{KT}$ ), (b) relaxation rate ( $\lambda_{AF}$ ), (c) precession frequency ( $f_{AF}$ ), (d) phase ( $\phi$ ), and (e) relaxation rates of the tail and the KT ( $\lambda_{tail}$  and  $\lambda_{KT}$ ). The solid line in panel (c) is a best fit obtained using  $f = f(0)(1 - T/T_N)^{\beta}$ :  $f(0) = 65.1(6)$  MHz,  $\beta = 0.279(7)$ , and  $T_N^{ZF} = 20.09(1)$  K.

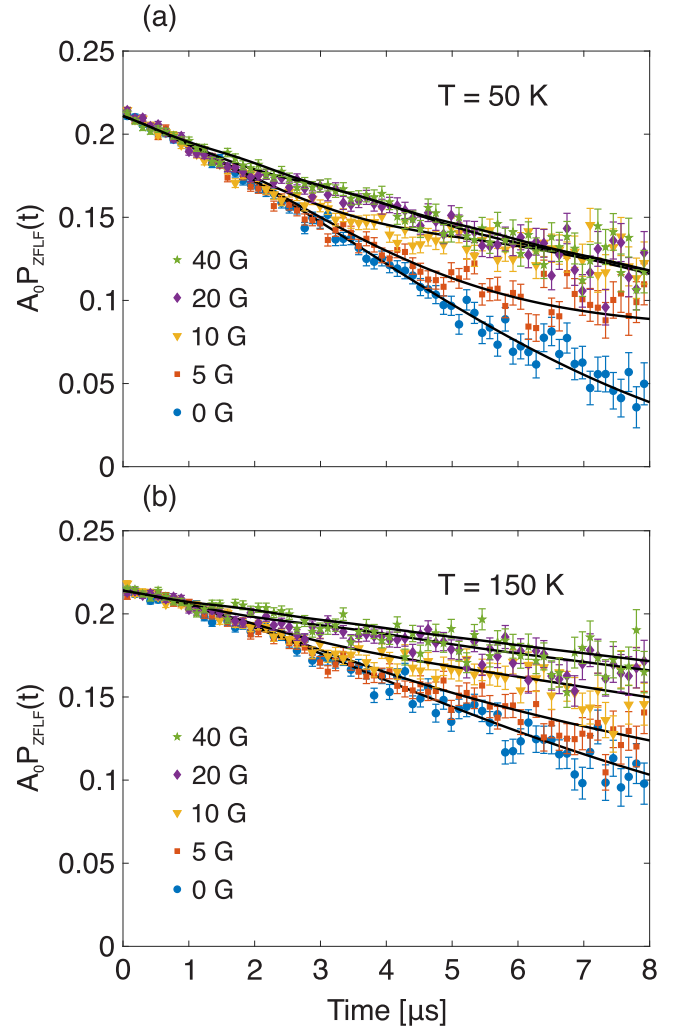


FIG. 6. Zero field and longitudinal field time spectrum collected at (a)  $T = 50$  K and (b)  $T = 150$  K. The solid lines represent the best fits using Eq. (3).

Therefore, besides electrochemical measurements, this is the first experimental indication of Na diffusion in  $\text{NaNiO}_2$ . We wish to emphasize that a more accurate way of measuring ion diffusion is to utilize a pulsed muon source, which is more suitable for detecting fluctuation of weak magnetic fields.

Here, we attempt to evaluate a self-diffusion coefficient of  $\text{Na}^+$  ions ( $D_{\text{Na}}$ ) using the present  $\mu^+$ SR result. Since the regular Na site is fully occupied by Na, the observed  $\nu$  naturally corresponds to a Na jump from a regular site to an interstitial site, i.e., to the center of the triangle formed by three Na [22,42]. Then,  $D_{\text{Na}}$  is given by [43]

$$D_{\text{Na}} = \sum_{i=1}^n \frac{1}{N_i} Z_{v,i} s_i^2 \nu, \quad (4)$$

where  $N_i$  is the number of Na sites in the  $i$ th path,  $Z_{v,i}$  is the vacancy fraction, and  $s_i$  is the jump distance. Based on the structure of  $\text{NaNiO}_2$ ,  $n = 1$ ,  $N_1 = 6$ ,  $Z_1 = 1$ , and  $s_1 = 1.707$  Å. Figure 8 displays  $\nu$  and  $D_{\text{Na}}$  as functions of inverse temperature in the temperature range between 100 and 175 K. The magnitude of  $D_{\text{Na}}$  at 300 K and the activation energy

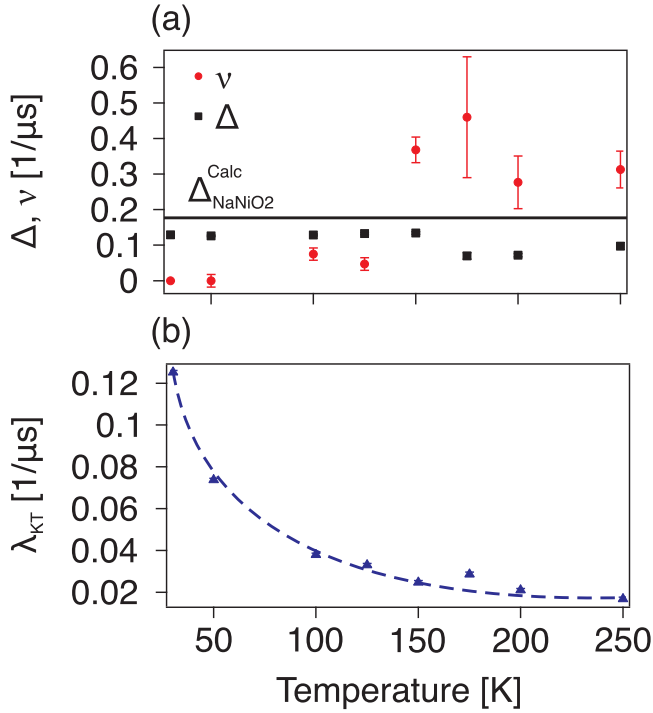


FIG. 7. Temperature dependence of fit parameters obtained using Eq. (2): (a) field distribution width ( $\Delta$ ) and field fluctuation rate ( $\nu$ ) and (b) relaxation rate ( $\lambda_{KT}$ ), where the broken line is a guide to the eye. The solid line in panel (a) represents the value of calculated  $\Delta$  at the muon site (0.624, 0, 0.854).

( $E_a$ ) for Na diffusion are estimated to  $8.8 \times 10^{-11}$  cm<sup>2</sup>/s and 50(20) meV, respectively. In this analysis, we have attributed the resulting  $\nu$  solely to Na-ion dynamics. Although, it should be mentioned that fluctuating Ni moments may induce additional relaxation of Na nuclear moments [30], which in turn affects the resulting  $\nu$  and thus  $D_{Na}$  and  $E_a$ . We hope a more detailed analysis will be carried out using data obtained at a pulsed muon facility.

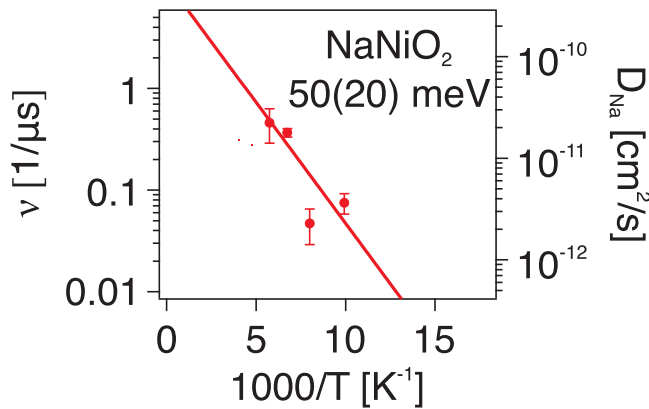


FIG. 8. The relationship between  $\nu$  [a diffusion coefficient of Na<sup>+</sup> ( $D_{Na}$ )] and inverse temperature for NaNiO<sub>2</sub>. The solid line represents the fit using a thermal activation process,  $\nu = \nu_0 \exp(-E_a/k_B T)$  in the temperature range between 100 and 175 K, where  $E_a$  is the activation energy and  $k_B$  is the Boltzmann constant.

#### IV. DISCUSSION

The internal field of NaNiO<sub>2</sub> is evaluated using Eq. (1) and compared to the obtained experimental values. As explained in Sec. I, the internal field for A-type antiferromagnets is composed of dipolar and possibly hyperfine contact terms. Each field component can be translated into a muon precession frequency via  $f = (\gamma_\mu/2\pi)|\mathbf{B}|$  such that

$$f_{loc} = (\gamma_\mu/2\pi)|\mathbf{B}_{dip'} + \mathbf{B}_{hf}|, \quad (5)$$

where  $f_{loc}$  is the calculated resulting muon precession frequency of the internal field where the experimentally obtained one [ $f_{AF}(T)$ ] is shown in Fig. 5(c),  $\mathbf{B}_{dip'}$  and  $\mathbf{B}_{hf}$  are the resulting internal field contributions of dipolar and hyperfine contact terms, respectively. It is noted that  $\mu^+$ SR detects only the magnitude of  $\mathbf{B}_{loc}$  so the final precession frequency is given by the modulus of Eq. (1).

The internal field calculations were done by MUESR [44] and DIPELEC [45], which have successfully replicated experimental results of antiferromagnetic [46–48], ferromagnetic [8,49], and incommensurate structures [50]. To correctly calculate the dipole field, the muon-dipole–electron-dipole interaction needs to be considered. However, a good approximation is to consider the spin-polarized electronic orbitals as classical dipoles located at the center of the magnetic atoms. In such a case, the dipolar field at the muon site is given by [3]

$$\mathbf{B}_{dip'} = \frac{\mu_0}{4\pi} \sum_j^N \frac{3\mathbf{r}_{\mu j}(\mathbf{m}_{e,j} \cdot \mathbf{r}_{\mu j})}{r_{\mu j}^5} - \frac{\mathbf{m}_{e,j}}{r_{\mu j}^3}, \quad (6)$$

where  $\mu_0$  is the vacuum permeability and contributions from all atoms are accounted up to a distance defined by  $N$ ;  $\mathbf{m}_{e,j} = -g_j\mu_B\mathbf{J}_j$ , where  $\mathbf{J}_j$  is the total angular momentum of the  $j$ th atom; and  $\mathbf{r}_{\mu,j}$  is the distance between the muon and the  $j$ th atom. A situation when  $N \rightarrow \infty$  yields  $\mathbf{B}_{dip'} \rightarrow \mathbf{B}_{dip}$ . The contact hyperfine field on the other hand accounts for the situation when the electron spin density is not 0 at the muon site. Principally, detailed information about the electron wave function is needed to correctly calculate  $\mathbf{B}_{hf}$ . Such estimations are impractical and some approximations are instead used. For one, the  $\mathbf{B}_{hf}$  is assumed to be isotropic, i.e., spherical electron wave functions at the muon site. For such a case,  $\mathbf{B}_{hf}$  is given by [3]

$$\mathbf{B}_{hf} = \frac{2\mu_0}{3} |\psi(\mathbf{r}_\mu)|^2 \mathbf{m}_e = \frac{2\mu_0}{3} \frac{\rho(\mathbf{r}_\mu)}{|\mathbf{m}_e|} \mathbf{m}_e, \quad (7)$$

where  $|\psi(\mathbf{r}_\mu)|^2$  is the probability density for a spherical electron cloud to be present at the muon site and  $\rho(\mathbf{r}_\mu)$  is the local spin density. Thus, a scalar coupling between  $\rho(\mathbf{r}_\mu)$  and  $\mathbf{m}_e$  is considered for the evaluation of  $\mathbf{B}_{hf}$ , where  $\mathbf{m}_e$  is the magnetic moment of the electron. Moreover, an average value is evaluated of the coupling from each magnetic neighboring atom, even though they may principally contribute with a different coupling.

In the previous study [9], it was pointed out that the internal field around the oxygen atoms in the octahedron could perhaps be explained by dipolar fields. However, the knowledge of the muon site is needed in order to properly evaluate Eqs. (6) and (7). Based on DFT calculations described in Sec. II, there are three possible muon sites,  $\mu 1$  at (0.624, 0, 0.854),  $\mu 2$  at

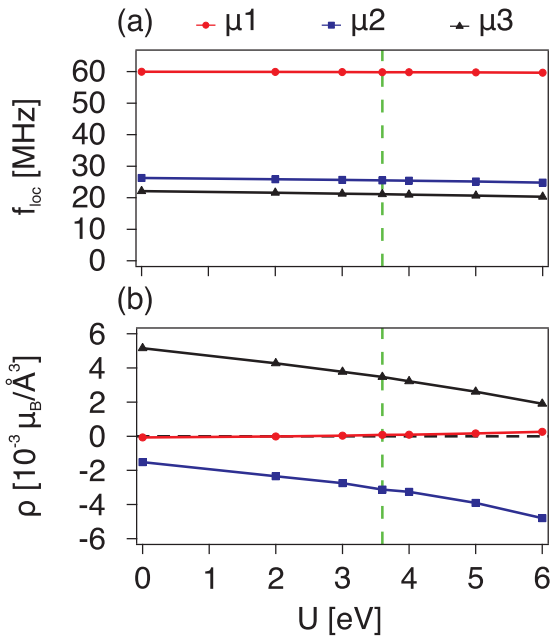


FIG. 9. The relationship between (a)  $f_{\text{loc}}$  and  $U$  and (b)  $\rho(\mathbf{r}_\mu)$  and  $U$  for the three muon sites:  $\mu 1$  at (0.624, 0, 0.854),  $\mu 2$  at (0.9467, 0, 0.28), and  $\mu 3$  at (0.84, 0.225, 0.69). The green vertical dashed line indicates  $U = 3.6$  eV, which was used for the data listed in Table I.

(0.9467, 0, 0.28), and  $\mu 3$  at (0.84, 0.225, 0.69), in the  $\text{NaNiO}_2$  lattice in the  $C2/m$  setting (unique  $b$  axis):  $a = 5.30811$ ,  $b = 2.84193$ ,  $c = 5.56671$  Å, and  $\beta = 110.4503^\circ$ . Moreover, the local spin densities at the given muon sites are calculated for the provided magnetic structure of Ref. [14]. Using the same magnetic structure with moments fully ordered within the  $ac$  plane with  $\mu_{\text{eff}} = 0.97 \mu_B$  ( $=|m_e|$ ), tilting  $100^\circ$  with respect to  $a$  axis, the results of Eq. (5) for each predicted site are listed in Table I.

Among the three muon sites,  $\mu 1$  at (0.624, 0, 0.854) provides a reasonable result to the experiment. The magnitude of  $\Delta$  for this site is also consistent with the experimental result (Fig. 7), suggesting indeed that the correct muon site is  $\mu 1$ . However, the calculated values of  $f_{\text{dip}'}$  ( $|\mathbf{B}_{\text{dip}'}| = |[-597, 0, -4380]| = (597^2 + 0^2 + 4380^2)^{0.5} = 4420$  G) and  $f_{\text{loc}}$  ( $|\mathbf{B}_{\text{dip}' + \mathbf{B}_{\text{hf}}}| = |[-597, 0, -4380] + [-1, 0, 6]| = [(-597-1)^2 + 0^2 + (-4380+6)^2]^{0.5} = 4414$  G) are close but not exactly  $f_{\text{AF}}(0)$ . Such discrepancy could be explained by use of slightly wrong values of lattice parameters, Ni moment, and/or  $\rho(\mathbf{r}_\mu)$  predicted by DFT calculations. The ambiguity of  $\rho(\mathbf{r}_\mu)$  could be caused by difficulty in determining the on-site electron-electron interaction energy  $U$  precisely [51]. However, only a small variation in  $f_{\text{loc}}$  is obtained for each site, when  $U$  is varied from 0 to 6 eV (see Fig. 9). More importantly, despite the introduction of  $\mathbf{B}_{\text{hf}}$ ,  $f_{\text{loc}}$  is not dramatically changed in the  $A$ -type AF,  $\text{NaNiO}_2$ , because the local spin density at the muon site is very small. Nevertheless,  $\mathbf{B}_{\text{hf}}$  is muon site dependent and could seriously alter  $f_{\text{loc}}$  for certain sites. In other words, even though the contribution of the hyperfine field to the precession frequency was not considered for analyzing the data in the previous work [9], the present work clarifies that such analysis happens to be acceptable. This is because the hyperfine field at the predicted

muon site is very small compared to the dipole field. Therefore, the  $\mu^+$ SR result on  $\text{NaNiO}_2$  has been tightly confirmed by the present work.

The determined muon site is most likely stable against the Na diffusion in the Na plane, since the muon site is located within the  $\text{NiO}_2$  plane. Many cathode materials for a Li-ion and Na-ion battery, such as  $\text{LiCoO}_2$  [25],  $\text{LiNiO}_2$  [37],  $\text{LiCo}_{1/3}\text{Ni}_{1/3}\text{Mn}_{1/3}\text{O}_2$  [52], and  $\text{NaCoO}_2$  [36], pose a similar layered structure. In these materials, it has been shown that the muon is stable against temperature and the dynamical effects are caused by Na and Li ions. However, it has been difficult to determine the muon site even with the help of DFT calculations, because of the lack of static magnetic order. Therefore, the determined muon site in the present work should be relevant for the abovementioned materials as well, given the similar layered structures. It is thus underlined that  $\mu^+$ SR is an applicable probe for detecting  $\text{Li}^+$  and  $\text{Na}^+$  diffusion since the muon site is stable against the ion diffusion.

## V. CONCLUSIONS

The internal magnetic field of the  $A$ -type antiferromagnet  $\text{NaNiO}_2$  has been studied by means of  $\mu^+$ SR. The muon site was predicted by DFT to (0.624, 0, 0.854), and such a site yielded internal field values consistent with the experiment in both antiferromagnetic and paramagnetic states. The presented results suggest that  $\mathbf{B}_{\text{hf}}$  does not significantly alter the total local field at the muon site, at least not in the  $A$ -type antiferromagnet  $\text{NaNiO}_2$ . However, since  $\mathbf{B}_{\text{hf}}$  is muon site dependent and sometimes difficult to deal with, it is desirable to perform similar studies on several  $A$ -type antiferromagnets to conclude whether the  $\mathbf{B}_{\text{hf}}$  contribution to the muon site is insignificant in  $A$ -type antiferromagnets. Finally, dynamic contributions from fluctuating nuclear moments were detected above 150 K, attributed to Na-ion dynamics. Its temperature dependence resembled a typical thermal activation process, yielding an activation energy of 50(20) meV and a diffusion coefficient at 300 K of  $8.8 \times 10^{-11}$  cm<sup>2</sup>/s.

## ACKNOWLEDGMENTS

We thank the staff of TRIUMF for help with the  $\mu^+$ SR experiment (M1251). All images involving crystal structure were made with the VESTA software [10]. O.K.F. and M.M. were partly supported by the Swedish Research Council (VR) through a neutron project grant (BIFROST, Grant No. Dnr. 2016-06955). H.O, C.M, and K.Y were supported by Japan Society for the Promotion Science (JSPS) KAKENHI Grant No. JP18KK0150. J.S was supported by JSPS KAKENHI Grant No. JP18H01863.

## APPENDIX: ZF FITTING PROCEDURES AT LOW TEMPERATURES

The ZF results presented in Sec. III B are very consistent with the previously published results of Ref. [9], particularly for the  $f_{\text{AF}}(T)$  curve. However, there is a minor discrepancy between the present and the previous results, namely, the missing asymmetry (explained in Sec. III B). If we use the described fitting procedure in Ref. [9], i.e., using two

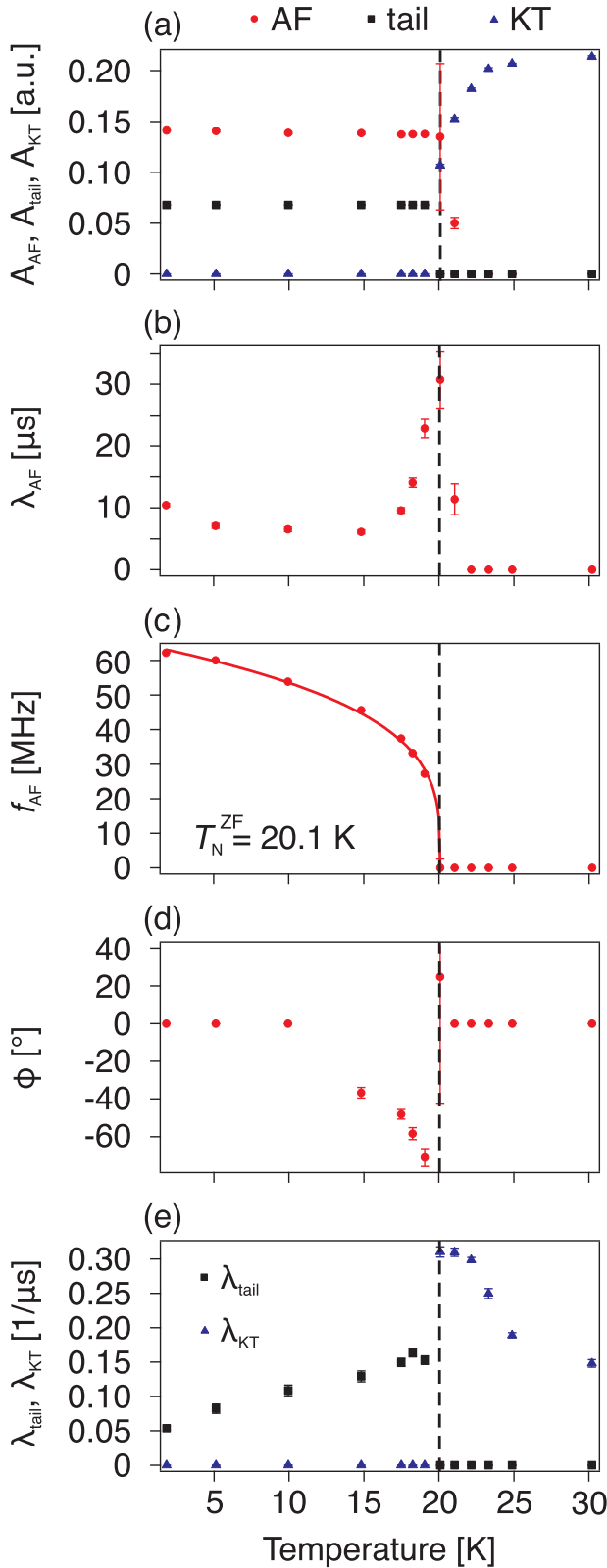


FIG. 10. Temperature dependencies of the fit parameters obtained with Eq. (3), but with fixed asymmetry sum: (a) asymmetries ( $A_{AF}$ ,  $A_{tail}$ , and  $A_{KT}$ ), (b) relaxation rate ( $\lambda_{AF}$ ), (c) precession frequency ( $f_{AF}$ ), (d) phase ( $\phi$ ), and (e) relaxation rates of the tail and the KT ( $\lambda_{tail}$  and  $\lambda_{KT}$ ). The solid line in panel (c) is a best fit obtained using  $f = f(0)(1 - T/T_N)^\beta$ :  $f(0) = 64.9(6)$  MHz,  $\beta = 0.278(8)$ , and  $T_N^{ZF} = 20.09(1)$  K.

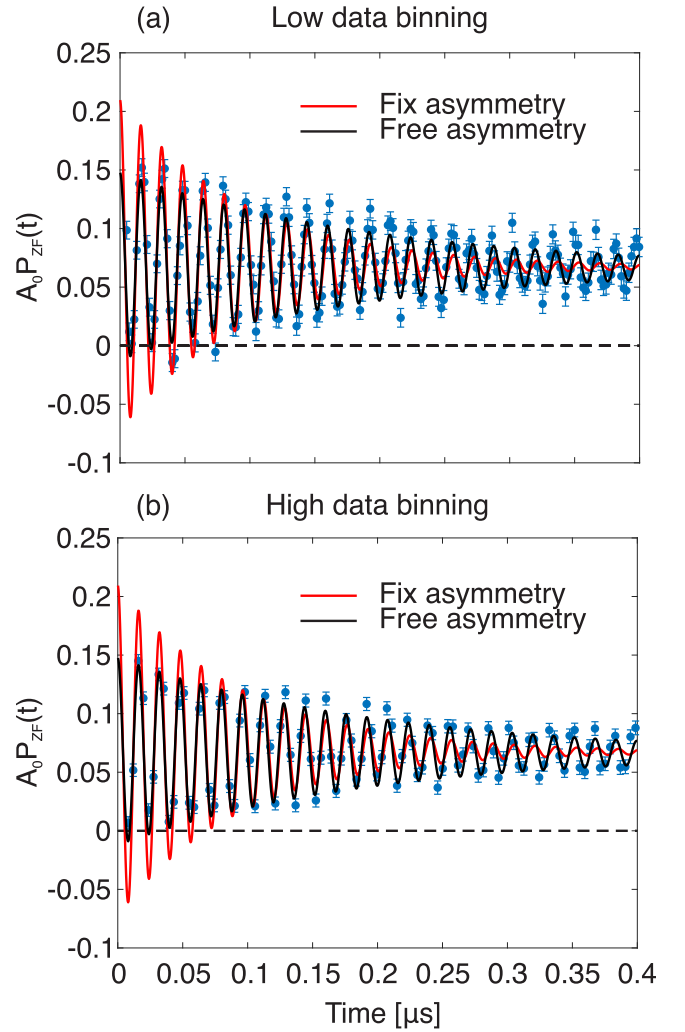


FIG. 11. Zero field (ZF) time spectra up to  $0.4 \mu\text{s}$  recorded at  $T = 2$  K, where the solid red lines are fits with the fixed asymmetry sum while the solid black lines are fits where the missing fraction is allowed. Such fits are shown with (a) low data binning and (b) high data binning.

asymmetries ( $A_{tail}$  and  $A_{AF}$ ) and fixing the sum, the missing asymmetry naturally disappears. This is because the missing asymmetry is no longer allowed since all available asymmetry is shared by  $A_{tail}$  and  $A_{AF}$ .

The temperature dependence of each fitting parameter obtained by such a fitting is shown in Fig. 10. The obtained results are identical to those of Fig. 5, except for the increase in  $A_{AF}$ . However, the reduced  $\chi^2$ , which MUSRFIT attempts to minimize during the fitting procedure, is  $\chi^2 = 1.037596$  for the “using two asymmetries and fixing the sum” approach, while the reduced  $\chi^2 = 1.017701$  for the “using three asymmetries” approach. The increase in the reduced  $\chi^2$  in the former approach is easily understood by closer inspection of the ZF time spectrum, as highlighted in Fig. 11. That is, in an early time domain, the fit result by the former approach provides an oscillation amplitude larger than that of the observed spectrum, resulting in a higher reduced  $\chi^2$ .

We have also studied the effect of binning of the data on the reduced  $\chi^2$ . As highlighted in Fig. 11(b), the two approaches look to yield equally satisfactory results, in cases where the data binning is too high. However, the fitting procedures for higher binned data returns a reduced  $\chi^2 = 1.346879$  and

1.120283 for the former and latter approaches, respectively. Considering the above factors, it is reasonable to assign the missing asymmetry observed in  $\text{NaNiO}_2$  as an intrinsic property, caused by wide and high fields and frequencies that cannot be resolved by  $\mu^+\text{SR}$ .

- 
- [1] A. Schenck, *Muon Spin Rotation Spectroscopy: Principles and Applications in Solid State Physics* (Taylor & Francis, Philadelphia, 1985).
- [2] G. M. Kalvius, D. R. Noakes, and O. Hartmann, *Handbook on the Physics and Chemistry of Rare Earths* (North-Holland, Amsterdam, 2001), Vol. 32, Chap. 206, pp. 55–451.
- [3] A. Yaouanc and P. D. de Réotier, *Muon Spin Rotation, Relaxation, and Resonance: Application to Condensed Matter* (Oxford, New York, 2011).
- [4] S. B. Sulaiman, S. Srinivas, N. Sahoo, F. Hagelberg, T. P. Das, E. Torikai, and K. Nagamine, *Phys. Rev. B* **49**, 9879 (1994).
- [5] M. Z. Uritskii and V. Y. Irkhin, *Phys. Solid State* **42**, 399 (2000).
- [6] S. J. Blundell, T. Lancaster, F. L. Pratt, P. J. Baker, W. Hayes, J.-P. Ansermet, and A. Comment, *Phys. Rev. B* **81**, 092407 (2010).
- [7] J. Sugiyama, H. Nozaki, M. Månsson, K. Prsa, D. Andreica, A. Amato, M. Isobe, and Y. Ueda, *Phys. Rev. B* **85**, 214407 (2012).
- [8] J. Sugiyama, K. Miwa, H. Nozaki, Y. Kaneko, B. Hitti, D. Arseneau, G. D. Morris, E. J. Ansaldo, and J. H. Brewer, *Phys. Rev. Mater.* **3**, 064402 (2019).
- [9] P. J. Baker, T. Lancaster, S. J. Blundell, M. L. Brooks, W. Hayes, D. Prabhakaran, and F. L. Pratt, *Phys. Rev. B* **72**, 104414 (2005).
- [10] K. Momma and F. Izumi, *J. Appl. Crystallogr.* **41**, 653 (2008).
- [11] S. Dick, M. Mübeller, F. Preissinger, and T. Zeiske, *Powder Diffr.* **12**, 239 (1997).
- [12] A. J. Reitsma, L. F. Feiner, and A. M. Oleś, *New J. Phys.* **7**, 121 (2005).
- [13] E. Chappel, M. D. Núñez-Regueiro, F. Dupont, G. Chouteau, C. Darie, and A. Sulpice, *Eur. Phys. J. B* **17**, 609 (2000).
- [14] C. Darie, P. Bordet, S. de Brion, M. Holzzapfel, O. Isnard, A. Lecchi, J. E. Lorenzo, and E. Suard, *Eur. Phys. J. B* **43**, 159 (2005).
- [15] M. V. Mostovoy and D. I. Khomskii, *Phys. Rev. Lett.* **89**, 227203 (2002).
- [16] J. Braconnier, C. Delmas, and P. Hagenmuller, *Mater. Res. Bull.* **17**, 993 (1982).
- [17] S. Miyazaki, S. Kikkawa, and M. Koizumi, *Synth. Met.* **6**, 211 (1983).
- [18] X. Wang, G. Liu, T. Iwao, M. Okubo, and A. Yamada, *J. Phys. Chem. C* **118**, 2970 (2014).
- [19] M. H. Han, E. Gonzalo, G. Singh, and T. Rojo, *Energy Environ. Sci.* **8**, 81 (2015).
- [20] J.-Y. Hwang, S.-T. Myung, and Y.-K. Sun, *Chem. Soc. Rev.* **46**, 3529 (2017).
- [21] X. Li, Y. Wang, D. Wu, L. Liu, S.-H. Bo, and G. Ceder, *Chem. Mater.* **28**, 6575 (2016).
- [22] J. Su, Y. Pei, Z. Yang, and X. Wang, *Comput. Mater. Sci.* **98**, 304 (2015).
- [23] C. V. Chandran and P. Heitjans, in *Annual Reports on NMR Spectroscopy*, edited by G. A. Webb (Academic, San Diego, 2016), Vol. 89, pp. 1–102.
- [24] C. P. Grey and N. Dupré, *Chem. Rev.* **104**, 4493 (2004).
- [25] J. Sugiyama, K. Mukai, Y. Ikedo, H. Nozaki, M. Månsson, and I. Watanabe, *Phys. Rev. Lett.* **103**, 147601 (2009).
- [26] A. Suter and B. M. Wojek, *Phys. Proc.* **30**, 69 (2012).
- [27] J. Kune, R. Arita, P. Wissgott, A. Toschi, H. Ikeda, and K. Held, *Comput. Phys. Commun.* **181**, 1888 (2010).
- [28] M. Dhariwal, T. Maitra, and I. Singh, in *Solid State Physics: Proceedings of the 57th DAE Solid State Physics Symposium 2012*, edited by A. K. Chauhan, C. Murli, and S. C. Gadkari, AIP Conf. Proc. No. 1512 (American Institute of Physics, New York, 2013), pp. 824–825.
- [29] P. Bonfá, and R. D. Renzi, *JPS Conf. Proc.* **85**, 091014 (2016).
- [30] T. Matsuzaki, K. Nishiyama, K. Nagamine, T. Yamazaki, M. Senba, J. M. Bailey, and J. H. Brewer, *Phys. Lett. A* **123**, 91 (1989).
- [31] C. Boekema, K. C. Chan, R. L. Lichti, A. B. Denison, D. W. Cooke, R. H. Heffner, R. L. Huston, and M. E. Schillaci, *Hyperfine Interact.* **32**, 667 (1986).
- [32] S. F. J. Cox, J. S. Lord, S. P. Cottrell, J. M. Gil, H. V. Alberto, A. Keren, D. Prabhakaran, R. Scheuermann, and A. Stoykov, *J. Phys.: Condens. Matter* **18**, 1061 (2006).
- [33] S. J. Blundell, T. Lancaster, P. J. Baker, W. Hayes, F. L. Pratt, T. Atake, D. S. Rana, and S. K. Malik, *Phys. Rev. B* **77**, 094424 (2008).
- [34] O. K. Forslund, *JPS Conf. Proc.* **21**, 011066 (2018).
- [35] J. Molenda and A. Stokłosa, *Solid State Ionics* **38**, 1 (1990).
- [36] M. Månsson and J. Sugiyama, *Phys. Scr.* **88**, 068509 (2013).
- [37] J. Sugiyama, Y. Ikedo, K. Mukai, H. Nozaki, M. Månsson, O. Ofer, M. Harada, K. Kamazawa, Y. Miyake, J. H. Brewer *et al.*, *Phys. Rev. B* **82**, 224412 (2010).
- [38] J. Sugiyama, K. Mukai, H. Nozaki, M. Harada, K. Kamazawa, M. Månsson, O. Ofer, E. J. Ansaldo, J. H. Brewer, K. H. Chow *et al.*, *Phys. Procedia* **30**, 105 (2012).
- [39] J. L. Gavilano, D. Rau, B. Pedrini, J. Hinderer, H. R. Ott, S. M. Kazakov, and J. Karpinski, *Phys. Rev. B* **69**, 100404(R) (2004).
- [40] M. Medarde, M. Mena, J. L. Gavilano, E. Pomjakushina, J. Sugiyama, K. Kamazawa, V. Yu. Pomjakushin, D. Sheptyakov, B. Batlogg, H. R. Ott, M. Månsson, and F. Juranyi, *Phys. Rev. Lett.* **110**, 266401 (2013).
- [41] H. W. Zandbergen, M. Foo, Q. Xu, V. Kumar, and R. J. Cava, *Phys. Rev. B* **70**, 024101 (2004).
- [42] R. Kaushalya, P. Iyngaran, N. Kuganathan, and A. Chreneos, *Energies* **12**, 3094 (2019).
- [43] R. J. Borg and G. J. Dienes, *An Introduction to Solid State Diffusion* (Academic, San Diego, 1988), Chap. 3, pp. 53–77.

- [44] P. Bonfá, I. J. Onuorah, and R. D. Renzi, *JPS Conf. Proc.* **21**, 011052 (2018).
- [45] K. M. Kojima, J. Yamanobe, H. Eisaki, S. Uchida, Y. Fudamoto, I. M. Gat, M. I. Larkin, A. Savici, Y. J. Uemura, P. P. Kyriakou *et al.*, *Phys. Rev. B* **70**, 094402 (2004).
- [46] R. De Renzi, G. Guidi, P. Podini, R. Tedeschi, C. Bucci, and S. F. J. Cox, *Phys. Rev. B* **30**, 186 (1984).
- [47] D. Vaknin, S. K. Sinha, D. E. Moncton, D. C. Johnston, J. M. Newsam, C. R. Safinya, and H. E. King, *Phys. Rev. Lett.* **58**, 2802 (1987).
- [48] J. Sugiyama, H. Nozaki, M. Harada, K. Kamazawa, O. Ofer, M. Månsson, J. H. Brewer, E. J. Ansaldo, K. H. Chow, Y. Ikeda *et al.*, *Phys. Rev. B* **84**, 054430 (2011).
- [49] M. Schmolz, K. P. Döring, K. Fürderer, M. Gladisch, N. Haas, D. Herlach, G. Majer, J. Rosenkranz, W. Schäfer, L. Schimmele *et al.*, *Hyperfine Interact.* **31**, 199 (1986).
- [50] A. Amato, P. Dalmas de Réotier, D. Andreica, A. Yaouanc, A. Suter, G. Lapertot, I. M. Pop, E. Morenzoni, P. Bonfà, F. Bernardini *et al.*, *Phys. Rev. B* **89**, 184425 (2014).
- [51] M. Cococcioni and S. de Gironcoli, *Phys. Rev. B* **71**, 035105 (2005).
- [52] J. Sugiyama, K. Mukai, M. Harada, H. Nozaki, K. Miwa, T. Shiotsuki, Y. Shindo, S. R. Giblin, and J. Lord, *Phys. Chem. Chem. Phys.* **15**, 10402 (2013).